

Measurement and Interpretation of UHECR Mass Composition at the Pierre Auger Observatory

Eric Mayotte^{a,*} for the Pierre Auger Collaboration^b

^a*Department of Physics, Colorado School of Mines, 1523 Illinois St., Golden CO, USA*

^b*Observatorio Pierre Auger, Av. San Martín Norte 304, 5613 Malargüe, Argentina*

Full author list: https://www.auger.org/archive/authors_icrc_2025.html

E-mail: spokespersons@auger.org

The Pierre Auger Observatory has driven the field of ultra-high-energy cosmic ray (UHECR) physics, producing several groundbreaking observations over the last 20 years. One of the most striking findings has been the complex evolution of UHECR mass composition, as revealed by detailed analyses of observables such as the depth of shower maximum (X_{\max}) and the muon content of showers. As more data are collected and sophisticated analyses are undertaken, not only are new fine details emerging, but the general picture of UHECR mass composition is becoming increasingly robust. This contribution presents recent results on the mass composition of UHECRs derived from surface, fluorescence, and radio detectors. Together with other key findings from the Observatory, these results converge to present a coherent picture of UHECR mass composition, effectively ruling out proton dominance and challenging the interpretation of the observed flux features as purely proton-induced propagation effects. To finish the contribution, we compare the X_{\max} data from the southern and northern equatorial bands of the exposure of the Pierre Auger Observatory fluorescence detector to evaluate the possibility of changes in composition as a function of declination.

*Speaker

Phase I and Phase II of the Pierre Auger Observatory

The Pierre Auger Observatory, located near the town of Malargüe, Mendoza, Argentina, sits at approximately 35.25° S, 69.3° W and has been observing ultra-high-energy cosmic ray (UHECR) air showers since January 1, 2004. Since its full completion in June 2008, it has been conducting precision measurements with 1660 Water Cherenkov Detector (WCD) stations, the Surface Detector (SD), and 27 fluorescence telescopes, the Fluorescence Detector (FD) [1]. The Observatory operated in this configuration until 2021, when the deployment of its major upgrade, AugerPrime [2], began.

The now-completed upgrade to the Observatory significantly increases statistics for mass composition studies at the highest energies through the addition of Surface Scintillator Detectors (SSDs) and Radio Detectors (RDs). The SSDs complement the WCDs to provide enhanced electromagnetic-muonic shower component separation up to a zenith angle of 60° . The RDs extend this sensitivity above 60° by measuring the electromagnetic component, while the WCDs measure the muons, which alone survive to the ground at high inclinations. A small PMT has been added in each WCD to enhance their dynamic range. Finally, SD electronics have been upgraded, providing improved timing resolution. The data collected before this upgrade constitute the Phase I dataset, while the data collected with the upgraded detector represent the Phase II dataset [3].

Herein, we present an overview of the current understanding of UHECR mass composition, based on data collected during Phase I of the Observatory. These include newly finalized FD measurements using the full Phase I dataset [4] and new data from a Universality-based SD reconstruction [5]. When these are added to the published measurements from the SD via neural networks [6] and the Auger Engineering Radio Array (AERA) [7], a detailed and consistent picture of the composition of UHECR comes into view. Finally, using the new higher statistics available in the FD, the composition of UHECRs in the southern and northern parts of the Observatory's exposure are directly compared to check for a declination dependence.

Measurements of the Depth of Shower Maximum

When a primary UHECR arrives at Earth and strikes a nucleus in the atmosphere, it triggers a complex cascade of secondary particles known as an extensive air shower (EAS). Early in the EAS, each collision of a secondary produces further secondaries, primarily pions (π^{\pm}, π^0) and kaons. The neutral π^0 quickly decays into pairs of photons, triggering electromagnetic sub-showers through processes like pair production and bremsstrahlung. The charged π^{\pm} and kaons either interact further, continuing the process, or decay to muons, creating the muonic component of the shower.

The evolution of the number of particles as a function of atmospheric depth (typically expressed in g/cm²) is referred to as the longitudinal profile of shower development. Early in the shower, the particle count grows rapidly as interactions with the atmosphere efficiently convert the initial kinetic energy of the primary into an exponential growth of secondary particles. This growth continues until the energy per particle falls below the threshold required to readily produce additional secondaries. At this critical point, the number of particles reaches its peak, the *Shower Maximum*. Beyond this point, secondary particle production is suppressed, and the shower progressively attenuates due to energy losses through ionization, bremsstrahlung, and decay processes, leading to a gradual reduction in particle count as the EAS penetrates deeper into the atmosphere.

The atmospheric depth at which this shower maximum occurs is called the *Depth of Shower*

Maximum (X_{\max}). X_{\max} is an important observable as it correlates strongly with the mass number, A , of a primary. As was laid out in [8], this strong correlation arises because, to first order, the length growth phase of the shower depends on the initial energy per nucleon of the primary. For a given primary energy, *light* primaries with lower A values will have higher per nucleon energies, leading to, on average, longer growth phases and higher X_{\max} values. *Heavy* primaries with higher A values, on the other hand, will, on average, have a shorter growth phase and lower X_{\max} values. However, due to nuclear modifications in nucleus-nucleus interactions, the superposition model is not exact. Numerically, the difference, $\langle X_{\max}(p, E_p) \rangle - \langle X_{\max}(A, E_p * A) \rangle$, can reach up to 10 g/cm^2 for iron-induced showers simulated with EPOS-LHC. It is also critical to note that the low particle count in the early stages of the EAS leads to sizable statistical fluctuations in the first few interactions, which carry into X_{\max} . This effect is fully present in light primaries, resulting in high fluctuations in X_{\max} . In contrast, at first interaction, heavy nuclei create up to A sub-showers which average out this effect, resulting in lower event-to-event variation in X_{\max} . Here, and more so than for $\langle X_{\max} \rangle$, variations in the nuclear fragmentation of a primary increase shower-to-shower fluctuations over what would be expected from the superposition model alone [9, 10]. As a result $\sigma(X_{\max})_A > \sigma(X_{\max})_p / \sqrt{A}$.

Except in extreme cases, X_{\max} can not be used to estimate the mass of the primary in a single shower due to these shower-by-shower fluctuations. Instead, typically, many X_{\max} measurements for events in a small energy range are gathered together into distributions of X_{\max} , whose statistical properties, typically their first and second moments, can then be used to estimate the average mass composition of measured UHECRs in that energy range. Since the last reporting of the combined X_{\max} measurements from the Observatory [11], the Phase I FD hybrid X_{\max} analysis has been finalized [4], and a Universality-based SD X_{\max} reconstruction has been carried out [5]. For details on the Universality reconstruction, the reader is encouraged to refer to the separate proceedings, which provide a comprehensive outline of the method and results [5]. The new FD hybrid measurement, described in [12], substantially improves both statistics and analysis. The Phase I hybrid dataset contains more than double the number of events of the 2014 X_{\max} PRD, allowing for the addition of new energy bins at high and low energies.

In comparison to the 2014 result, the Phase I FD Hybrid analysis uses a more accurate parameterization of atmospheric aerosols [13], an improved method of fitting the shower profile [14], and new parameterizations of the fiducial field of view cuts, acceptance, bias, resolution, and systematics [12]. These changes have resulted in an, on average, $\sim 5 \text{ g/cm}^2$ shift in reconstructed X_{\max} to higher values. This difference can be seen in the black points in Fig. 1 on the left, which shows the mean difference between the new FD hybrid X_{\max} reconstruction, the 2014 FD X_{\max} measurement [15], and the SD DNN X_{\max} reconstruction [6]. Because the DNN-based SD X_{\max}

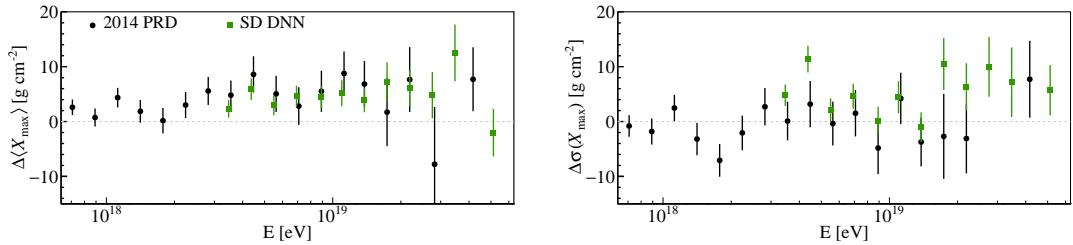


Figure 1: Comparison of the Phase I FD X_{\max} measurements [4] to those published in the 2014 FD hybrid and the 2024 SD DNN analyses. Left: first moment, $\langle X_{\max}^{\text{new}} \rangle - \langle X_{\max}^{\text{other}} \rangle$. Right: second moment $\sigma(X_{\max}^{\text{new}}) - \sigma(X_{\max}^{\text{other}})$.

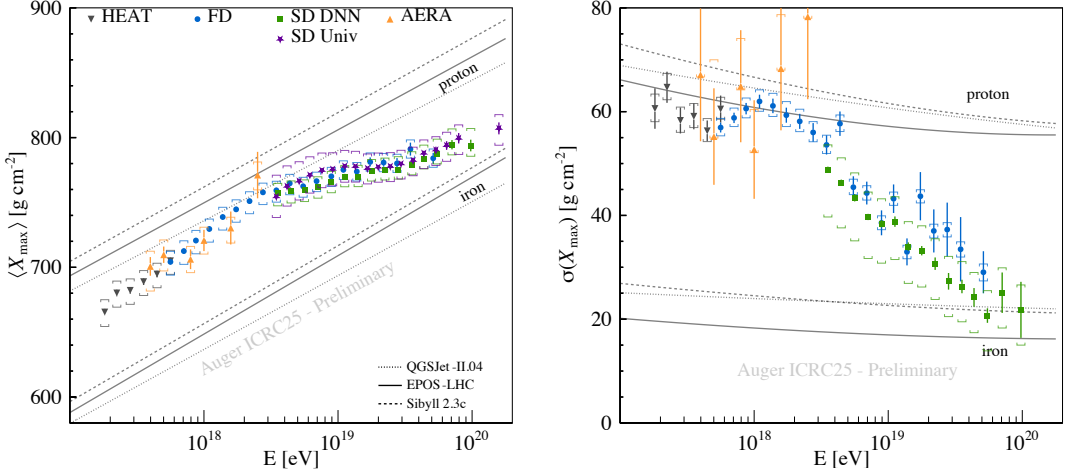


Figure 2: The first (left) and second (right) moments of X_{\max} distributions measured with the FD [4], the SD [5, 6], AERA [7] during Phase I. Preliminary measurements from HEAT [17] are also shown.

analysis was calibrated using the old FD hybrid reconstruction to remove the effects of the hadronic interaction model it was trained on, it also inherited the old FD X_{\max} scale and the $\sim 5 \text{ g/cm}^2$ difference. Notably for $\sigma(X_{\max})$, no difference is seen between the 2014 FD measurement and the new results; however, there is an apparent difference with the SD DNN. The FD result consistency rules out changes in FD analysis as a cause. Instead, the difference is likely due to the large SD DNN systematic uncertainties in $\sigma(X_{\max})$ and residual model or methodological dependencies.

The most up-to-date summary of the latest X_{\max} measurements made using FD Hybrid [4], SD [5, 6], and AERA [7, 16] data are shown together in Fig. 2. Preliminary measurements from High Elevation Auger Telescopes (HEAT) [17] are also included. Despite progressive updates to reconstruction methods that introduce varying X_{\max} scales in the FD, HEAT, AERA, and SD measurements, the $\langle X_{\max} \rangle$ values obtained show outstanding consistency at all energies. $\sigma(X_{\max})$ is more complex, and the 18.6–18.7 $\lg(E/\text{eV})$ energy bin of the hybrid data in particular stands out. This energy bin contains a deep outlier event. Its removal would decrease $\sigma(X_{\max})$ by $\sim 2 \text{ g/cm}^2$ bringing the moment closer to the overall trend (see [4] for details). Additionally, $\sigma(X_{\max})$ for SD Universality has been omitted due to ongoing work correcting for its resolution (see [5]).

The Overall Picture of Mass Composition

Much information on the mass composition of UHECRs can be gleaned directly from the moments of X_{\max} shown in Fig. 2. That said, it is useful to process the X_{\max} moments and distributions further to extract a fuller picture. Two practical approaches are to transform the moments of X_{\max} into moments of $\ln(A)$ (the logarithm of the primary mass) [18] and to fit the fractional contribution of different mass groups to the flux using the X_{\max} distributions measured at each energy [19].

From [18], the conversion of $\langle X_{\max} \rangle$ and $\sigma(X_{\max})$ into $\langle \ln(A) \rangle$ and $V(\ln(A))$ uses Hadronic Interaction Models (HIMs) to set the X_{\max} scale and parametrize its fluctuations as

$$\langle \ln(A) \rangle = \frac{\langle X_{\max} \rangle - \langle X_{\max} \rangle_p}{f_E}, \quad (1)$$

where $\langle X_{\max} \rangle_p$ is the mean X_{\max} for protons at the relevant energy in the chosen HIM, and

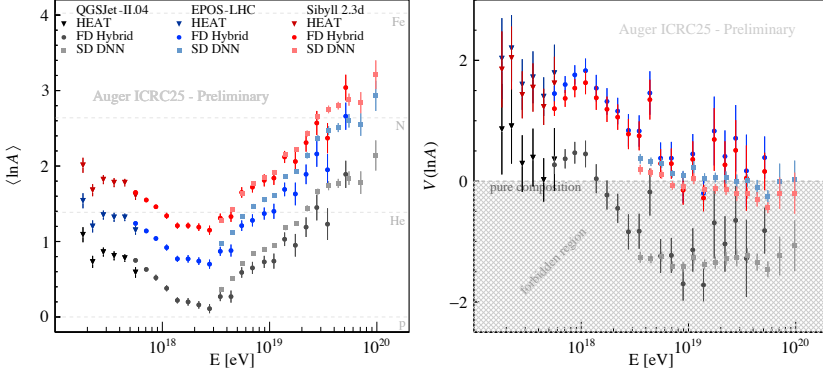


Figure 3: The first (left) and second (right) moments of $\ln A$ distributions derived from the FD [4] and SD Phase I [6] X_{\max} moments in Fig. 2 using QGSJet-II.04 (grey) [20], EPOS-LHC (blue) [21], and Sibyll 2.3d (red) [22].

$f_E = (\langle X_{\max} \rangle_{Fe} - \langle X_{\max} \rangle_p) / \ln(56)$. $V(\ln(A))$, in turn, is calculated as

$$V(\ln(A)) = \frac{\sigma^2(X_{\max}) - \sigma_{sh}^2(\langle \ln(A) \rangle)}{b \sigma_p^2 - f_E^2}, \quad (2)$$

where $\sigma_{sh}^2(\langle \ln(A) \rangle)$ is the HIM prediction of the X_{\max} variance for the $\langle \ln(A) \rangle$ value found at this energy, and σ_p^2 is the HIM X_{\max} variance prediction for proton; b is a fit parameter. This procedure is applied to the FD [4], SD DNN [6], and HEAT [17] results in Fig. 2 using EPOS-LHC, Sibyll 2.3d and QGSJET-II.04. The resulting moments of $\ln(A)$ are shown in Fig. 3.

As can be seen, the first and second moments of X_{\max} and $\ln(A)$ provide a clear summary of the overall UHECR composition. However, they do not offer a clear picture of the individual contributions of distinct mass groups. By generating templates of the X_{\max} distributions for proton, helium, nitrogen, and iron with HIMs, and then fitting a superposition of these templates to the measured X_{\max} distributions at each energy, estimates of the fractional abundances of each mass group can be extracted [19]. This procedure has been applied to the Phase I hybrid FD data [4] and preliminary HEAT data [17] in Fig. 4.

It should be emphasized that the above results depend on the HIMs used and that many new models and model tweaks are under development, which are expected to modify the X_{\max} scale and its variations meaningfully. These, in turn, are expected

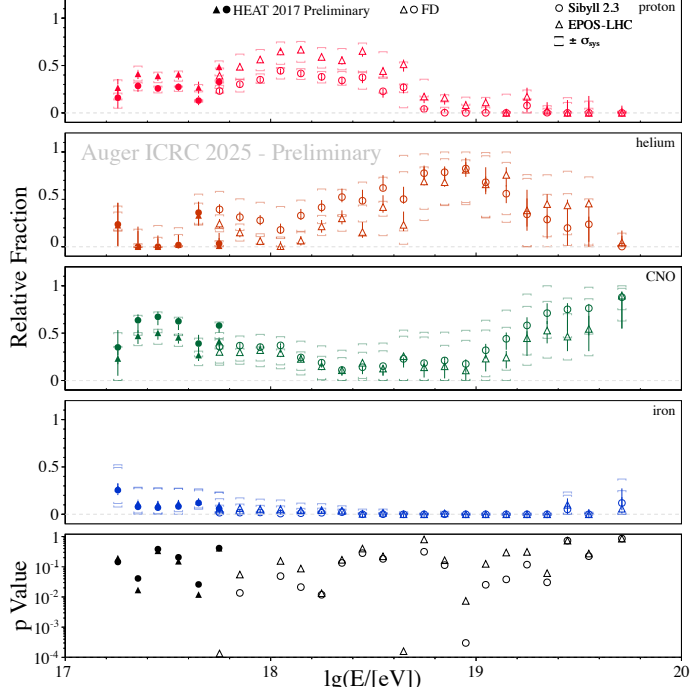


Figure 4: UHECR fractional mass composition derived from FD [4] and preliminary HEAT data [17]. Estimated using Sibyll 2.3 (HEAT), Sibyll 2.3d, and EPOS-LHC. QGSJet-II.04 has been omitted as it produces unphysical results (see Fig. 3 for example). For details on the fits / analysis and fits with new models, see [4].

to alter the details shown in Fig. 3 and Fig. 4 (see [4]). However, in addition to the above methods, there are other techniques, for example, the comparison of SD signals in X_{\max} (see [23]) and close examinations of the energy evolution of $\langle X_{\max} \rangle$ and $\sigma(X_{\max})$ [24], which can inform trends without reliance on HIMs for interpretation. By applying all these approaches to the accumulated data from Phase I of the Observatory, a clear and consistent picture of the mass composition of UHECRs emerges. Above $10^{17.2}$ eV, the arriving composition of the UHECR flux can be generally characterized by the following principal behaviors:

1. **Predominantly hadronic primaries:** Nearly all UHECR primaries are protons or heavier atomic nuclei, as no definitive observations of other particle types have yet been made [25, 26].
2. **Non-monotonic evolution with energy:** As energy increases, average nuclear mass decreases until reaching a minimum near 3 EeV. Afterward, it rises steadily with energy (Fig. 3) [4].
3. **Structured evolution with energy:** The evolution of X_{\max} with energy shows structure with changes seen around 2 EeV with the FD [4, 15] and 6.5, 11, and 31 EeV with the SD ([5, 24]).
4. **Changing composition purity:** For most energies, the composition flux of UHECR is mixed, often with multiple adjacent mass groups present simultaneously (Fig. 4 and [23]). Above a few EeV, the degree of mixing in the UHECR beam starts to decrease. Past ~ 10 EeV, the flux at any single energy becomes increasingly dominated by species within a narrow range of masses (Fig. 3 right and [6]).

X_{\max} in the Southern and Northern Skies

Due to the size of the Phase I hybrid dataset, it is now possible to split the sky into northern and southern regions in declination and carry out a preliminary independent X_{\max} analysis on both. By comparing the X_{\max} measurements of these two sky regions, we can directly test whether UHECR composition varies with declination within the Observatory's exposure. The split between the northern and southern regions is made at a declination of -15.7° , which was chosen as it represents the southernmost extent of the FD hybrid composition sensitivity of Telescope Array [27]. The exposure of the hybrid X_{\max} Phase I dataset of the Pierre Auger Observatory, with a line indicating the northern and southern data split, is shown on the left of Fig. 5. In contrast, the relative counts in each energy bin are shown on the right of Fig. 5.

To compare the mass composition in these two regions, the same analysis as was carried out for the FD hybrid data in Fig. 2 was performed here. However, for this analysis, separate investigations and corrections were carried out for each region to account for acceptance, reconstruction bias,

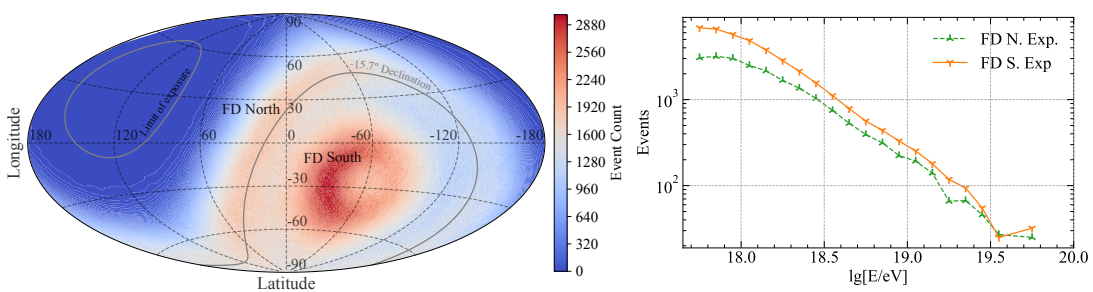


Figure 5: Northern and southern equatorial band definitions and counts. Left: FD Exposure with the -15.7° declination dividing line of the analysis split shown. Right: the relative counts of the analysis.

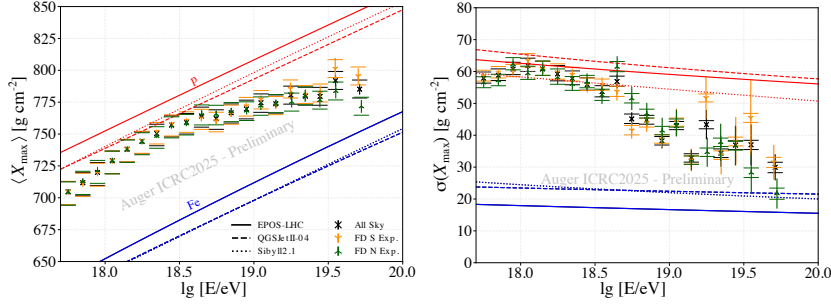


Figure 6: The first (left) and second (right) moments of the X_{\max} distributions from northern (green) and southern (orange) analysis regions. The black points represent the measurement over the full sky.

resolution, and systematics, following the methods described in [28]. The differences in reconstruction bias, resolution, and other systematics were found to be small. Because the distributions of shower zenith in the two regions differed, the X_{\max} dependent event acceptance also differed. This acceptance was extracted using simulation, and its effects were corrected for using the Λ_n method described in [15]. Residual uncertainties between the two regions from this correction are less than 2 g/cm^2 . The resulting moments of the X_{\max} distributions measured in each energy bin of the two regions are shown in Fig. 6.

Fig. 6 left shows that there is excellent bin-to-bin agreement between the northern and southern skies for $\langle X_{\max} \rangle$. In Fig. 6, right, there is good statistical agreement for the majority of energies. Some differences in the moments do appear at high energies where statistics become poor. To gauge whether any significant bin-by-bin differences occur between the two regions, the Kolmogorov-Smirnov [29] (KS) and Anderson-Darling [30] (AD) 2-sample tests are used to compare the two distributions in each energy bin in Fig. 7.

The results of the KS and AD tests indicate that the mass composition in the northern and southern regions is consistent with each other across the full energy range on a bin-by-bin basis. Larger differences are seen in the last two energy bins with the KS (AD) test reporting a Test Statistic (TS) of 0.29 (0.56) and 0.39 (3.72) for the second-to-last and last energy bins, respectively. For reference, the reduced χ^2 for these bins are 1.6 and 3.0. These KS (AD) values convert to local p-values of 0.016 (0.206) and 0.0003 (0.011) and global p-values of 0.322 (0.989) and 0.006 (0.20) for the second-to-last and last energy bins, respectively. With the current statistics, the differences seen in these two bins are not globally significant. This finding is in agreement with an earlier 2021 analysis, which found no evidence for a difference in the elongation rates and hence mass changes in published data taken in both hemispheres over multiple years [31]. This result is also in full agreement with the work of the Pierre Auger Observatory/Telescope Array working group on mass composition, which found no tension in the mass measurements of the two Observatories [32]. Further checks for differences between the northern and southern equatorial bands will be performed in the future with better statistics via SD and Phase II analyses.

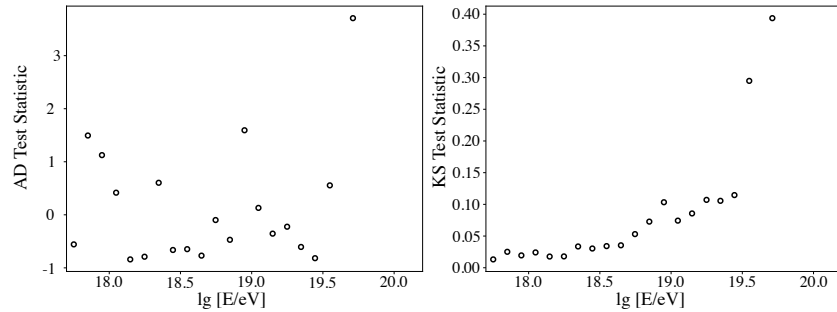


Figure 7: The results of KS (left) and AD (right) 2-sample tests between the X_{\max} distributions from northern and southern analysis regions.

Conclusion

After nearly two decades of data taking, the Pierre Auger Observatory has amassed the most comprehensive dataset on UHECRs to date. Through the careful analysis of this data, the overall knowledge of the composition of arriving UHECRs has vastly improved. Within the limitations of our current Hadronic Interaction Models, we now know that UHECRs consist of many atomic nuclei species, ranging from protons to possibly up to iron nuclei. Their mass composition is mixed, evolves strongly with energy, and may have fine-grained features, similar to those observed in the spectrum. The ankle is not heavily dominated by protons, and flux trends toward heavy at the highest energies. To evaluate the possibility of a meaningful difference in mean composition between the northern and southern skies, the Phase I FD hybrid data were split at -15.7° declination. When independent composition analyses were conducted on the two resulting equatorial bands, no significant differences in composition were found.

References

- [1] A. Aab et al., [Pierre Auger Coll.], *Nucl. Instrum. Meth. A* **798** (2015) 172 [[1502.01323](#)].
- [2] A. Aab et al., [Pierre Auger Coll.], [1604.03637](#).
- [3] A. Castellina, [Pierre Auger Coll.], *EPJ Web Conf.* **210** (2019) 06002 [[1905.04472](#)].
- [4] Pierre Auger Collaboration, *Phys. Rev. D* (2025) in preparation.
- [5] M. Stadelmeyer, [Pierre Auger Coll.], *PoS(ICRC2025)* These proceedings.
- [6] A. Abdul Halim et al., [Pierre Auger Coll.], *Phys. Rev. D* **111** (2025) 022003 [[2406.06319](#)].
- [7] A. Abdul Halim et al., [Pierre Auger Coll.], *Phys. Rev. D* **109** (2024) 022002 [[2310.19966](#)].
- [8] K.-H. Kampert and M. Unger, *AP* **35** (2012) 660.
- [9] J. Engel, T.K. Gaisser, T. Stanev and P. Lipari, *Phys. Rev. D* **46** (1992) 5013.
- [10] N.N. Kalmykov and S.S. Ostapchenko, *Phys. Atom. Nucl.* **56** (1993) 346.
- [11] E. Mayotte et al., [Pierre Auger Coll.], *PoS ICRC2023* (2023) 365.
- [12] P. Abreu et al., [Pierre Auger Coll.], *PoS ICRC2023* (2023) 319.
- [13] V.M. Harvey et al., [Pierre Auger Coll.], *PoS ICRC2023* (2023) 300.
- [14] J. Bellido et al., [Pierre Auger Coll.], *PoS ICRC2023* (2023) 211.
- [15] A. Aab et al., [Pierre Auger Coll.], *Phys. Rev. D* **90** (2014) 122005 [[1409.4809](#)].
- [16] A. Abdul Halim et al., [Pierre Auger Coll.], *Phys. Rev. Lett.* **132** (2024) 021001 [[2310.19963](#)].
- [17] J. Bellido, [Pierre Auger Coll.], *PoS ICRC2017* (2018) 506.
- [18] P. Abreu et al., [Pierre Auger Coll.], *JCAP* **02** (2013) 026 [[1301.6637](#)].
- [19] A. Aab et al., [Pierre Auger Coll.], *Phys. Rev. D* **90** (2014) 122006 [[1409.5083](#)].
- [20] S. Ostapchenko, *Phys. Rev. D* **83** (2011) 014018 [[1010.1869](#)].
- [21] T. Pierog, *PoS ICRC2017* (2018) 1100.
- [22] F. Riehn et al., *PoS ICRC2017* (2018) 301 [[1709.07227](#)].
- [23] A. Yushkov, [Pierre Auger Coll.], *PoS(ICRC2025)* These proceedings.
- [24] A. Abdul Halim et al., [Pierre Auger Coll.], *Phys. Rev. Lett.* **134** (2025) 021001 [[2406.06315](#)].
- [25] N. González, [Pierre Auger Coll.], *PoS UHECR2024* (2025) 023.
- [26] J. Alvarez-Muñiz, [Pierre Auger Coll.], *PoS UHECR2024* (2025) 025.
- [27] R.U. Abbasi et al., [Telescope Array Coll.], *Astrophys. J.* **858** (2018) 76 [[1801.09784](#)].
- [28] E. Mayotte et al., [Pierre Auger Coll.], *PoS ICRC2021* (2021) 321.
- [29] F.J. Massey Jr, *JASA* **46** (1951) 68.
- [30] F.W. Scholz and M.A. Stephens, *JASA* **82** (1987) 918.
- [31] A.A. Watson, *JHEAp* **33** (2022) 14 [[2112.06525](#)].
- [32] A. Abdul Halim et al., [Pierre Auger and Telescope Array Coll.], *PoS ICRC2023* (2023) 249.

The Pierre Auger Collaboration



PIERRE
AUGER
OBSERVATORY

- A. Abdul Halim¹³, P. Abreu⁷⁰, M. Aglietta^{53,51}, I. Allekotte¹, K. Almeida Cheminant^{78,77}, A. Almela^{7,12}, R. Aloisio^{44,45}, J. Alvarez-Muñiz⁷⁶, A. Ambrosone⁴⁴, J. Ammerman Yebra⁷⁶, G.A. Anastasi^{57,46}, L. Anchordoqui⁸³, B. Andrade⁷, L. Andrade Dourado^{44,45}, S. Andringa⁷⁰, L. Apollonio^{58,48}, C. Aramo⁴⁹, E. Arnone^{62,51}, J.C. Arteaga Velázquez⁶⁶, P. Assis⁷⁰, G. Avila¹¹, E. Avocone^{56,45}, A. Bakalova³¹, F. Barbato^{44,45}, A. Bartz Mocellin⁸², J.A. Bellido¹³, C. Berat³⁵, M.E. Bertaina^{62,51}, M. Bianciotto^{62,51}, P.L. Biermann^a, V. Binet⁵, K. Bismarck^{38,7}, T. Bister^{77,78}, J. Biteau^{36,i}, J. Blazek³¹, J. Blümer⁴⁰, M. Boháčová³¹, D. Boncioli^{56,45}, C. Bonifazi⁸, L. Bonneau Arbeletche²², N. Borodai⁶⁸, J. Brack^f, P.G. Brichetto Orchera^{7,40}, F.L. Brieche⁴¹, A. Bueno⁷⁵, S. Buitink¹⁵, M. Buscemi^{46,57}, M. Büskens^{38,7}, A. Bwembya^{77,78}, K.S. Caballero-Mora⁶⁵, S. Cabana-Freire⁷⁶, L. Caccianiga^{58,48}, F. Campuzano⁶, J. Caraça-Valente⁸², R. Caruso^{57,46}, A. Castellina^{53,51}, F. Catalani¹⁹, G. Cataldi⁴⁷, L. Cazon⁷⁶, M. Cerda¹⁰, B. Čermáková⁴⁰, A. Cermenati^{44,45}, J.A. Chinellato²², J. Chudoba³¹, L. Chytka³², R.W. Clay¹³, A.C. Cobos Cerutti⁶, R. Colalillo^{59,49}, R. Conceição⁷⁰, G. Consolati^{48,54}, M. Conte^{55,47}, F. Convenga^{44,45}, D. Correia dos Santos²⁷, P.J. Costa⁷⁰, C.E. Covault⁸¹, M. Cristinziani⁴³, C.S. Cruz Sanchez³, S. Dasso^{4,2}, K. Daumiller⁴⁰, B.R. Dawson¹³, R.M. de Almeida²⁷, E.-T. de Boone⁴³, B. de Errico²⁷, J. de Jesús⁷, S.J. de Jong^{77,78}, J.R.T. de Mello Neto²⁷, I. De Miti^{44,45}, J. de Oliveira¹⁸, D. de Oliveira Franco⁴², F. de Palma^{55,47}, V. de Souza²⁰, E. De Vito^{55,47}, A. Del Popolo^{57,46}, O. Deligny³³, N. Denner³¹, L. Deval^{53,51}, A. di Matteo⁵¹, C. Dobrigkeit²², J.C. D'Olivo⁶⁷, L.M. Domingues Mendes^{16,70}, Q. Dorost⁴³, J.C. dos Anjos¹⁶, R.C. dos Anjos²⁶, J. Ebr³¹, F. Ellwanger⁴⁰, R. Engel^{38,40}, I. Epicoco^{55,47}, M. Erdmann⁴¹, A. Etchegoyen^{7,12}, C. Evoli^{44,45}, H. Falcke^{77,79,78}, G. Farrar⁸⁵, A.C. Fauth²², T. Fehler⁴³, F. Feldbusch³⁹, A. Fernandes⁷⁰, M. Fernandez¹⁴, B. Fick⁸⁴, J.M. Figueira⁷, P. Filip^{38,7}, A. Filipčič^{74,73}, T. Fitoussi⁴⁰, B. Flagg⁸⁷, T. Fodran⁷⁷, A. Franco⁴⁷, M. Freitas⁷⁰, T. Fujii^{86,h}, A. Fuster^{7,12}, C. Galea⁷⁷, B. García⁶, C. Gaudu³⁷, P.L. Ghia³³, U. Giaccari⁴⁷, F. Gobbi¹⁰, F. Gollan⁷, G. Golup¹, M. Gómez Berisso¹, P.F. Gómez Vitale¹¹, J.P. Gongora¹¹, J.M. González¹, N. González⁷, D. Góra⁶⁸, A. Gorgi^{53,51}, M. Gottowik⁴⁰, F. Guarino^{59,49}, G.P. Guedes²³, L. Gültzow⁴⁰, S. Hahn³⁸, P. Hamal³¹, M.R. Hampel⁷, P. Hansen³, V.M. Harvey¹³, A. Haungs⁴⁰, T. Hebbeker⁴¹, C. Hojvat^d, J.R. Hörandel^{77,78}, P. Horvath³², M. Hrabovsky³², T. Huege^{40,15}, A. Insolia^{57,46}, P.G. Isar⁷², M. Ismaiel^{77,78}, P. Janecek³¹, V. Jilek³¹, K.-H. Kampert³⁷, B. Keilhauer⁴⁰, A. Khakurdikar⁷⁷, V.V. Kizakke Covilakam^{7,40}, H.O. Klages⁴⁰, M. Kleifges³⁹, J. Köhler⁴⁰, F. Krieger⁴¹, M. Kubatova³¹, N. Kunka³⁹, B.L. Lago¹⁷, N. Langner⁴¹, N. Leal⁷, M.A. Leigui de Oliveira²⁵, Y. Lema-Capeans⁷⁶, A. Letessier-Selvon³⁴, I. Lhenry-Yvon³³, L. Lopes⁷⁰, J.P. Lundquist⁷³, M. Mallamaci^{60,46}, D. Mandat³¹, P. Mantsch^d, F.M. Mariani^{58,48}, A.G. Mariazzi³, I.C. Mariş¹⁴, G. Marsella^{60,46}, D. Martello^{55,47}, S. Martinelli^{40,7}, M.A. Martins⁷⁶, H.-J. Mathes⁴⁰, J. Matthews^g, G. Matthiae^{61,50}, E. Mayotte⁸², S. Mayotte⁸², P.O. Mazur^d, G. Medina-Tanco⁶⁷, J. Meinert³⁷, D. Melo⁷, A. Menshikov³⁹, C. Merx⁴⁰, S. Michal³¹, M.I. Micheletti⁵, L. Miramonti^{58,48}, M. Mogarkar⁶⁸, S. Mollerach¹, F. Montanet³⁵, L. Morejon³⁷, K. Mulrey^{77,78}, R. Mussa⁵¹, W.M. Namasaka³⁷, S. Negi³¹, L. Nellen⁶⁷, K. Nguyen⁸⁴, G. Nicora⁹, M. Niechciol⁴³, D. Nitz⁸⁴, D. Nosek³⁰, A. Novikov⁸⁷, V. Novotny³⁰, L. Nožka³², A. Nucita^{55,47}, L.A. Núñez²⁹, J. Ochoa^{7,40}, C. Oliveira²⁰, L. Östman³¹, M. Palatka³¹, J. Pallotta⁹, S. Panja³¹, G. Parente⁷⁶, T. Paulsen³⁷, J. Pawlowsky³⁷, M. Pech³¹, J. Pěkala⁶⁸, R. Pelayo⁶⁴, V. Pelgrims¹⁴, L.A.S. Pereira²⁴, E.E. Pereira Martins^{38,7}, C. Pérez Bertolli^{7,40}, L. Perrone^{55,47}, S. Petrera^{44,45}, C. Petrucci⁵⁶, T. Pierog⁴⁰, M. Pimenta⁷⁰, M. Platino⁷, B. Pont⁷⁷, M. Pourmohammad Shahvar^{60,46}, P. Privitera⁸⁶, C. Priyadarshi⁶⁸, M. Prouza³¹, K. Pytel⁶⁹, S. Querchfeld³⁷, J. Rautenberg³⁷, D. Ravignani⁷, J.V. Reginatto Akim²², A. Reuzki⁴¹, J. Ridky³¹, F. Riehn^{76,j}, M. Risso⁴³, V. Rizi^{56,45}, E. Rodriguez^{7,40}, G. Rodriguez Fernandez⁵⁰, J. Rodriguez Rojo¹¹, S. Rossoni⁴², M. Roth⁴⁰, E. Roulet¹, A.C. Rovero⁴, A. Saftoiu⁷¹, M. Saharan⁷⁷, F. Salamida^{56,45}, H. Salazar⁶³, G. Salina⁵⁰, P. Sampathkumar⁴⁰, N. San Martin⁸², J.D. Sanabria Gomez²⁹, F. Sánchez⁷, E.M. Santos²¹, E. Santos³¹, F. Sarazin⁸², R. Sarmento⁷⁰, R. Sato¹¹, P. Savina^{44,45}, V. Scherini^{55,47}, H. Schieler⁴⁰, M. Schimassee³³, M. Schimp³⁷, D. Schmidt⁴⁰, O. Scholten^{15,b}, H. Schoorlemmer^{77,78}, P. Schovánek³¹, F.G. Schröder^{87,40}, J. Schulte⁴¹, T. Schulz³¹, S.J. Sciutto³, M. Scornavacche⁷, A. Sedoski⁷, A. Segreto^{52,46}, S. Sehgal³⁷, S.U. Shivashankara⁷³, G. Sigl¹⁴²,

K. Simkova^{15,14}, F. Simon³⁹, R. Šmídá⁸⁶, P. Sommers^e, R. Squartini¹⁰, M. Stadelmaier^{40,48,58}, S. Stanič⁷³, J. Stasielak⁶⁸, P. Stassi³⁵, S. Strähn³⁸, M. Straub⁴¹, T. Suomijärvi³⁶, A.D. Supanitsky⁷, Z. Svozilíkova³¹, K. Syrokvas³⁰, Z. Szadkowski⁶⁹, F. Tairli¹³, M. Tambone^{59,49}, A. Tapia²⁸, C. Taricco^{62,51}, C. Timmermans^{78,77}, O. Tkachenko³¹, P. Tobiska³¹, C.J. Todero Peixoto¹⁹, B. Tomé⁷⁰, A. Travaini¹⁰, P. Travnicek³¹, M. Tueros³, M. Unger⁴⁰, R. Uzeiroska³⁷, L. Vaclavek³², M. Vacula³², I. Vaiman^{44,45}, J.F. Valdés Galicia⁶⁷, L. Valore^{59,49}, P. van Dillen^{77,78}, E. Varela⁶³, V. Vaščková³⁷, A. Vásquez-Ramírez²⁹, D. Veberič⁴⁰, I.D. Vergara Quispe³, S. Verpoest⁸⁷, V. Verzi⁵⁰, J. Vicha³¹, J. Vink⁸⁰, S. Vorobiov⁷³, J.B. Vuta³¹, C. Watanabe²⁷, A.A. Watson^c, A. Weindl⁴⁰, M. Weitz³⁷, L. Wiencke⁸², H. Wilczyński⁶⁸, B. Wundheiler⁷, B. Yue³⁷, A. Yushkov³¹, E. Zas⁷⁶, D. Zavrtanik^{73,74}, M. Zavrtanik^{74,73}

————— • —————

- ¹ Centro Atómico Bariloche and Instituto Balseiro (CNEA-UNCuyo-CONICET), San Carlos de Bariloche, Argentina
- ² Departamento de Física and Departamento de Ciencias de la Atmósfera y los Océanos, FCEyN, Universidad de Buenos Aires and CONICET, Buenos Aires, Argentina
- ³ IFLP, Universidad Nacional de La Plata and CONICET, La Plata, Argentina
- ⁴ Instituto de Astronomía y Física del Espacio (IAFE, CONICET-UBA), Buenos Aires, Argentina
- ⁵ Instituto de Física de Rosario (IFIR) – CONICET/U.N.R. and Facultad de Ciencias Bioquímicas y Farmacéuticas U.N.R., Rosario, Argentina
- ⁶ Instituto de Tecnologías en Detección y Astropartículas (CNEA, CONICET, UNSAM), and Universidad Tecnológica Nacional – Facultad Regional Mendoza (CONICET/CNEA), Mendoza, Argentina
- ⁷ Instituto de Tecnologías en Detección y Astropartículas (CNEA, CONICET, UNSAM), Buenos Aires, Argentina
- ⁸ International Center of Advanced Studies and Instituto de Ciencias Físicas, ECyT-UNSAM and CONICET, Campus Miguelete – San Martín, Buenos Aires, Argentina
- ⁹ Laboratorio Atmósfera – Departamento de Investigaciones en Láseres y sus Aplicaciones – UNIDEF (CITEDEF-CONICET), Argentina
- ¹⁰ Observatorio Pierre Auger, Malargüe, Argentina
- ¹¹ Observatorio Pierre Auger and Comisión Nacional de Energía Atómica, Malargüe, Argentina
- ¹² Universidad Tecnológica Nacional – Facultad Regional Buenos Aires, Buenos Aires, Argentina
- ¹³ University of Adelaide, Adelaide, S.A., Australia
- ¹⁴ Université Libre de Bruxelles (ULB), Brussels, Belgium
- ¹⁵ Vrije Universiteit Brussels, Brussels, Belgium
- ¹⁶ Centro Brasileiro de Pesquisas Físicas, Rio de Janeiro, RJ, Brazil
- ¹⁷ Centro Federal de Educação Tecnológica Celso Suckow da Fonseca, Petropolis, Brazil
- ¹⁸ Instituto Federal de Educação, Ciência e Tecnologia do Rio de Janeiro (IFRJ), Brazil
- ¹⁹ Universidade de São Paulo, Escola de Engenharia de Lorena, Lorena, SP, Brazil
- ²⁰ Universidade de São Paulo, Instituto de Física de São Carlos, São Carlos, SP, Brazil
- ²¹ Universidade de São Paulo, Instituto de Física, São Paulo, SP, Brazil
- ²² Universidade Estadual de Campinas (UNICAMP), IFGW, Campinas, SP, Brazil
- ²³ Universidade Estadual de Feira de Santana, Feira de Santana, Brazil
- ²⁴ Universidade Federal de Campina Grande, Centro de Ciencias e Tecnologia, Campina Grande, Brazil
- ²⁵ Universidade Federal do ABC, Santo André, SP, Brazil
- ²⁶ Universidade Federal do Paraná, Setor Palotina, Palotina, Brazil
- ²⁷ Universidade Federal do Rio de Janeiro, Instituto de Física, Rio de Janeiro, RJ, Brazil
- ²⁸ Universidad de Medellín, Medellín, Colombia
- ²⁹ Universidad Industrial de Santander, Bucaramanga, Colombia
- ³⁰ Charles University, Faculty of Mathematics and Physics, Institute of Particle and Nuclear Physics, Prague, Czech Republic
- ³¹ Institute of Physics of the Czech Academy of Sciences, Prague, Czech Republic
- ³² Palacky University, Olomouc, Czech Republic
- ³³ CNRS/IN2P3, IJCLab, Université Paris-Saclay, Orsay, France

- ³⁴ Laboratoire de Physique Nucléaire et de Hautes Energies (LPNHE), Sorbonne Université, Université de Paris, CNRS-IN2P3, Paris, France
- ³⁵ Univ. Grenoble Alpes, CNRS, Grenoble Institute of Engineering Univ. Grenoble Alpes, LPSC-IN2P3, 38000 Grenoble, France
- ³⁶ Université Paris-Saclay, CNRS/IN2P3, IJCLab, Orsay, France
- ³⁷ Bergische Universität Wuppertal, Department of Physics, Wuppertal, Germany
- ³⁸ Karlsruhe Institute of Technology (KIT), Institute for Experimental Particle Physics, Karlsruhe, Germany
- ³⁹ Karlsruhe Institute of Technology (KIT), Institut für Prozessdatenverarbeitung und Elektronik, Karlsruhe, Germany
- ⁴⁰ Karlsruhe Institute of Technology (KIT), Institute for Astroparticle Physics, Karlsruhe, Germany
- ⁴¹ RWTH Aachen University, III. Physikalisches Institut A, Aachen, Germany
- ⁴² Universität Hamburg, II. Institut für Theoretische Physik, Hamburg, Germany
- ⁴³ Universität Siegen, Department Physik – Experimentelle Teilchenphysik, Siegen, Germany
- ⁴⁴ Gran Sasso Science Institute, L'Aquila, Italy
- ⁴⁵ INFN Laboratori Nazionali del Gran Sasso, Assergi (L'Aquila), Italy
- ⁴⁶ INFN, Sezione di Catania, Catania, Italy
- ⁴⁷ INFN, Sezione di Lecce, Lecce, Italy
- ⁴⁸ INFN, Sezione di Milano, Milano, Italy
- ⁴⁹ INFN, Sezione di Napoli, Napoli, Italy
- ⁵⁰ INFN, Sezione di Roma “Tor Vergata”, Roma, Italy
- ⁵¹ INFN, Sezione di Torino, Torino, Italy
- ⁵² Istituto di Astrofisica Spaziale e Fisica Cosmica di Palermo (INAF), Palermo, Italy
- ⁵³ Osservatorio Astrofisico di Torino (INAF), Torino, Italy
- ⁵⁴ Politecnico di Milano, Dipartimento di Scienze e Tecnologie Aerospaziali , Milano, Italy
- ⁵⁵ Università del Salento, Dipartimento di Matematica e Fisica “E. De Giorgi”, Lecce, Italy
- ⁵⁶ Università dell’Aquila, Dipartimento di Scienze Fisiche e Chimiche, L’Aquila, Italy
- ⁵⁷ Università di Catania, Dipartimento di Fisica e Astronomia “Ettore Majorana“, Catania, Italy
- ⁵⁸ Università di Milano, Dipartimento di Fisica, Milano, Italy
- ⁵⁹ Università di Napoli “Federico II”, Dipartimento di Fisica “Ettore Pancini”, Napoli, Italy
- ⁶⁰ Università di Palermo, Dipartimento di Fisica e Chimica ”E. Segrè”, Palermo, Italy
- ⁶¹ Università di Roma “Tor Vergata”, Dipartimento di Fisica, Roma, Italy
- ⁶² Università Torino, Dipartimento di Fisica, Torino, Italy
- ⁶³ Benemérita Universidad Autónoma de Puebla, Puebla, México
- ⁶⁴ Unidad Profesional Interdisciplinaria en Ingeniería y Tecnologías Avanzadas del Instituto Politécnico Nacional (UPIITA-IPN), México, D.F., México
- ⁶⁵ Universidad Autónoma de Chiapas, Tuxtla Gutiérrez, Chiapas, México
- ⁶⁶ Universidad Michoacana de San Nicolás de Hidalgo, Morelia, Michoacán, México
- ⁶⁷ Universidad Nacional Autónoma de México, México, D.F., México
- ⁶⁸ Institute of Nuclear Physics PAN, Krakow, Poland
- ⁶⁹ University of Łódź, Faculty of High-Energy Astrophysics, Łódź, Poland
- ⁷⁰ Laboratório de Instrumentação e Física Experimental de Partículas – LIP and Instituto Superior Técnico – IST, Universidade de Lisboa – UL, Lisboa, Portugal
- ⁷¹ “Horia Hulubei” National Institute for Physics and Nuclear Engineering, Bucharest-Magurele, Romania
- ⁷² Institute of Space Science, Bucharest-Magurele, Romania
- ⁷³ Center for Astrophysics and Cosmology (CAC), University of Nova Gorica, Nova Gorica, Slovenia
- ⁷⁴ Experimental Particle Physics Department, J. Stefan Institute, Ljubljana, Slovenia
- ⁷⁵ Universidad de Granada and C.A.F.P.E., Granada, Spain
- ⁷⁶ Instituto Galego de Física de Altas Enerxías (IGFAE), Universidade de Santiago de Compostela, Santiago de Compostela, Spain
- ⁷⁷ IMAPP, Radboud University Nijmegen, Nijmegen, The Netherlands
- ⁷⁸ Nationaal Instituut voor Kernfysica en Hoge Energie Fysica (NIKHEF), Science Park, Amsterdam, The Netherlands
- ⁷⁹ Stichting Astronomisch Onderzoek in Nederland (ASTRON), Dwingeloo, The Netherlands
- ⁸⁰ Universiteit van Amsterdam, Faculty of Science, Amsterdam, The Netherlands

- ⁸¹ Case Western Reserve University, Cleveland, OH, USA
⁸² Colorado School of Mines, Golden, CO, USA
⁸³ Department of Physics and Astronomy, Lehman College, City University of New York, Bronx, NY, USA
⁸⁴ Michigan Technological University, Houghton, MI, USA
⁸⁵ New York University, New York, NY, USA
⁸⁶ University of Chicago, Enrico Fermi Institute, Chicago, IL, USA
⁸⁷ University of Delaware, Department of Physics and Astronomy, Bartol Research Institute, Newark, DE, USA
-

- ^a Max-Planck-Institut für Radioastronomie, Bonn, Germany
^b also at Kapteyn Institute, University of Groningen, Groningen, The Netherlands
^c School of Physics and Astronomy, University of Leeds, Leeds, United Kingdom
^d Fermi National Accelerator Laboratory, Fermilab, Batavia, IL, USA
^e Pennsylvania State University, University Park, PA, USA
^f Colorado State University, Fort Collins, CO, USA
^g Louisiana State University, Baton Rouge, LA, USA
^h now at Graduate School of Science, Osaka Metropolitan University, Osaka, Japan
ⁱ Institut universitaire de France (IUF), France
^j now at Technische Universität Dortmund and Ruhr-Universität Bochum, Dortmund and Bochum, Germany

Acknowledgments

The successful installation, commissioning, and operation of the Pierre Auger Observatory would not have been possible without the strong commitment and effort from the technical and administrative staff in Malargüe. We are very grateful to the following agencies and organizations for financial support:

Argentina – Comisión Nacional de Energía Atómica; Agencia Nacional de Promoción Científica y Tecnológica (ANPCyT); Consejo Nacional de Investigaciones Científicas y Técnicas (CONICET); Gobierno de la Provincia de Mendoza; Municipalidad de Malargüe; NDM Holdings and Valle Las Leñas; in gratitude for their continuing cooperation over land access; Australia – the Australian Research Council; Belgium – Fonds de la Recherche Scientifique (FNRS); Research Foundation Flanders (FWO), Marie Curie Action of the European Union Grant No. 101107047; Brazil – Conselho Nacional de Desenvolvimento Científico e Tecnológico (CNPq); Financiadora de Estudos e Projetos (FINEP); Fundação de Amparo à Pesquisa do Estado de Rio de Janeiro (FAPERJ); São Paulo Research Foundation (FAPESP) Grants No. 2019/10151-2, No. 2010/07359-6 and No. 1999/05404-3; Ministério da Ciência, Tecnologia, Inovações e Comunicações (MCTIC); Czech Republic – GACR 24-13049S, CAS LQ100102401, MEYS LM2023032, CZ.02.1.01/0.0/0.0/16_013/0001402, CZ.02.1.01/0.0/0.0/18_046/0016010 and CZ.02.1.01/0.0/0.0/17_049/0008422 and CZ.02.01.01/00/22_008/0004632; France – Centre de Calcul IN2P3/CNRS; Centre National de la Recherche Scientifique (CNRS); Conseil Régional Ile-de-France; Département Physique Nucléaire et Corpusculaire (PNC-IN2P3/CNRS); Département Sciences de l'Univers (SDU-INSU/CNRS); Institut Lagrange de Paris (ILP) Grant No. LABEX ANR-10-LABX-63 within the Investissements d'Avenir Programme Grant No. ANR-11-IDEX-0004-02; Germany – Bundesministerium für Bildung und Forschung (BMBF); Deutsche Forschungsgemeinschaft (DFG); Finanzministerium Baden-Württemberg; Helmholtz Alliance for Astroparticle Physics (HAP); Helmholtz-Gemeinschaft Deutscher Forschungszentren (HGF); Ministerium für Kultur und Wissenschaft des Landes Nordrhein-Westfalen; Ministerium für Wissenschaft, Forschung und Kunst des Landes Baden-Württemberg; Italy – Istituto Nazionale di Fisica Nucleare (INFN); Istituto Nazionale di Astrofisica (INAF); Ministero dell'Università e della Ricerca (MUR); CETEMPS Center of Excellence; Ministero degli Affari Esteri (MAE), ICSC Centro Nazionale di Ricerca in High Performance Computing, Big Data and Quantum Computing, funded by European Union NextGenerationEU, reference code CN_00000013; México – Consejo Nacional de Ciencia y Tecnología (CONACYT) No. 167733; Universidad Nacional Autónoma de México (UNAM); PAPIIT DGAPA-UNAM; The Netherlands – Ministry of Education, Culture and Science; Netherlands Organisation for Scientific Research (NWO); Dutch national e-infrastructure with the support of SURF Cooperative; Poland – Ministry of Education and Science, grants No. DIR/WK/2018/11 and 2022/WK/12; National Science Centre, grants No. 2016/22/M/ST9/00198, 2016/23/B/ST9/01635, 2020/39/B/ST9/01398, and 2022/45/B/ST9/02163; Portugal – Portuguese national funds and FEDER funds within Programa Operacional Factores de Competitividade through Fundação para a Ciência e a Tecnologia (COMPETE); Romania – Ministry of Research, Innovation and Digitization, CNCS-UEFISCDI, contract no. 30N/2023 under Romanian National Core Program LAPLAS VII, grant no. PN 23 21

01 02 and project number PN-III-P1-1.1-TE-2021-0924/TE57/2022, within PNCDI III; Slovenia – Slovenian Research Agency, grants P1-0031, P1-0385, I0-0033, N1-0111; Spain – Ministerio de Ciencia e Innovación/Agencia Estatal de Investigación (PID2019-105544GB-I00, PID2022-140510NB-I00 and RYC2019-027017-I), Xunta de Galicia (CIGUS Network of Research Centers, Consolidación 2021 GRC GI-2033, ED431C-2021/22 and ED431F-2022/15), Junta de Andalucía (SOMM17/6104/UGR and P18-FR-4314), and the European Union (Marie Skłodowska-Curie 101065027 and ERDF); USA – Department of Energy, Contracts No. DE-AC02-07CH11359, No. DE-FR02-04ER41300, No. DE-FG02-99ER41107 and No. DE-SC0011689; National Science Foundation, Grant No. 0450696, and NSF-2013199; The Grainger Foundation; Marie Curie-IRSES/EPLANET; European Particle Physics Latin American Network; and UNESCO.